

Effect of Dynamic and Preferential Decoration of Pt Catalyst Surfaces by WO_x on Hydrodeoxygenation Reactions

Justin Marlowe^{1,†}, Siddharth Deshpande^{2,3,†}, Dionisios G. Vlachos^{2,3*}, Mahdi M. Abu-Omar^{1,4*}, Phillip Christopher^{1*}

1. Department of Chemical Engineering, University of California Santa Barbara, Santa Barbara, CA 93106, United States
2. Department of Chemical and Biomolecular Engineering, University of Delaware, Newark, DE 19716, United States
3. Catalysis Center for Energy Innovation, University of Delaware, Newark, DE 19716, United States
4. Department of Chemistry and Biochemistry, University of California Santa Barbara, Santa Barbara, CA 93106, United States

[†] these authors contributed equally to this work.

* corresponding author

* Dionisios G. Vlachos: vlachos@udel.edu, Mahdi M. Abu-Omar: mabuomar@ucsb.edu, Phillip Christopher: pchristopher@ucsb.edu,

Abstract: Metal-support interactions are important in the design of supported metal catalysts. Recently, catalysts containing Pt nanoparticles and reducible transition metal oxides (WO_x , NbO_x , TiO_x) have been demonstrated to exhibit remarkable selectivity to aromatic products in hydrodeoxygenation (HDO) reactions for biomass valorization, contrasting the undesired aromatic hydrogenation typically observed for metal catalysts. However, the active structure responsible for the enhanced catalysis remains unknown. Here, theoretical and experimental analyses are combined to explain the observed HDO reactivity by describing the organization of reduced WO_x domains on Pt surfaces at sub-monolayer coverage. The SurfGraph algorithm is used to develop DFT models that capture the configurational space (~ 1000 configurations) of a W_3O_7 trimer on stepped Pt surfaces. ML-DFT models predict preferential occupation of well-coordinated Pt sites (≥ 8 Pt coordination number) by WO_x and identify structural features governing WO_x -Pt stability. $\text{WO}_x/\text{Pt}/\text{SiO}_2$ catalysts are synthesized with varying W loading to test the theoretical predictions and relate them to HDO reactivity. Spectroscopy- and microscopy-based catalyst characterization identifies the dynamic and preferential decoration of well-coordinated sites on Pt nanoparticles by reduced WO_x species, consistent with theoretical predictions. The consequences of this preferential decoration on the HDO of dihydroeugenol (DHE), a lignin model compound, are clarified. The modifying effect of WO_x decoration on Pt nanoparticles for HDO involves WO_x inhibiting aromatic ring hydrogenation by preferentially blocking well-coordinated Pt sites. The identification of preferential decoration on specific sites of late transition metal surfaces by reducible metal oxides provides a new perspective for understanding and controlling metal-support interactions in heterogeneous catalysis.

Keywords: Density functional theory, Graph theory, Machine learning, Catalysts, Hydrodeoxygenation, Restructuring, Platinum, Tungsten, Structure-activity relationship

Introduction

Metal nanoparticles stabilized on oxide supports are ubiquitous heterogeneous catalysts for chemical conversions. One particularly interesting class of supported metal catalysts is Pt-group metal nanoparticles supported on reducible transition metal oxides, where strong chemical and physical metal-support interactions can mediate reactivity. For example, Tauster *et al.* in the late 1970's used Pt/TiO₂^{1,2} to highlight changes in reactivity and chemisorption capacity in response to high-temperature (>500°C) treatments in H₂ atmospheres that are reversible through re-oxidation by O₂. The reducible support was shown to play a crucial role in the observed behavior, deduced by comparison to irreducible Pt/Al₂O₃ and Pt/SiO₂ catalysts, earning this phenomenon the title of “strong metal-support interaction” (SMSI). Extensive work since then has identified the dynamic formation of reduced oxide overlayers on the metal surface³⁻⁶, thought to be driven by a reduction in surface free energy⁷, resulting in altered catalytic activity and chemisorption capacity due to formation of an oxide overlayer blocking metallic sites and the introduction of new oxide-metal interfaces.

Recently, a new class of analogous materials deemed “inverse catalysts” have been reported⁸⁻¹². These materials are composed of unsupported or irreducible (e.g. Al₂O₃, C, SiO₂) oxide-supported metal nanoparticles onto which reducible (Fe₃O₄, TiO₂, etc.) oxide domains are co-deposited, often through intentional, synthetic routes. The reducible oxide layers can overcoat the Pt group metal nanoparticles, akin to the overcoating seen in SMSI. An important feature of inverse catalysts in comparison to traditional SMSI catalysts (e.g. Pt/TiO₂), wherein the reducible support is present in a significant stoichiometric excess relative to the metal nanoparticles, is the tunable coverage of the reducible oxide on the metal based on the amount reducible metal oxide added, providing an additional dial to modify catalyst activity.

Inverse catalysts can exhibit significantly altered reaction kinetics as compared to the bare metal catalysts^{4,13-15}, with an important application being hydrodeoxygenation (HDO) of lignin-derived monomers towards biomass valorization¹⁶⁻¹⁸. For example, inverse catalysts such as WO_x/Pt/C and NbO_x/Pt/MgAl₂O₄ achieve >98% selectivity to desirable deoxygenated aromatics, in stark contrast to their unmodified analogues that exhibit considerable aromatic hydrogenation activity to produce undesired products with saturated rings. Recently, we reported on the structure sensitivity of Pt catalysts for HDO of model lignin-derived phenolic monomers, identifying that low-index terraces, consisting of well-coordinated Pt (Pt_{TC}) atoms, are responsible for the undesired aromatic hydrogenation reaction¹⁹. Considering the likely co-existence of covered and uncovered metal sites on the surface of inverse catalysts for HDO, it is thus essential to elucidate the extent to which specific surface Pt sites, such as Pt_{TC} sites, become decorated by reducible metal oxide domains in order to understand the role of oxide overcoating in altering catalyst performance.

The organization of reducible oxide domains on the surfaces of metal nanoparticles, as seen in inverse catalysts, specifically with an appreciation of potential metal site-specificity (e.g. steps vs terraces), remains elusive, particularly under reaction conditions. Surface science studies of reducible oxide overcoating of metal single crystals have demonstrated the formation of oxide “trails” or dendrites, suggestive of facile surface diffusion of oxide species^{20,21}. Further, it has been observed that oxide growth nucleates at metallic step sites, suggestive of energetic stabilization of

oxide domains at specific locations on metal surfaces^{22–26}. However, these effects have not been resolved for nanoparticle surfaces under reaction conditions. Additionally, theoretical analyses have primarily focused on low-index metal surfaces, which has limited applicability to the inherently defective surfaces of nanoparticles found in heterogeneous catalysts that expose steps, edges, and corners.

Herein, we theoretically assess the organization and stability of a model W_3O_7 trimer on various stepped Pt surfaces using density functional theory (DFT) and a new machine learning protocol. We combine these computational studies with electron microscopy, *in-situ* and probe molecule spectroscopies, and HDO reactivity measurements to elucidate the dynamic, site-dependent organization of WO_x overcoating domains on Pt nanoparticle surfaces in heterogeneous inverse $WO_x/Pt/SiO_2$ catalysts. The computational and experimental results identify the preferential decoration of well-coordinated Pt sites (terraces) by WO_x as the primary contributor to suppressed hydrogenation of the aromatic ring in HDO of phenolics on inverse catalysts. The identification of preferential decoration of specific metal sites by reducible oxide domains extends the knowledge on inverse catalysts previously limited to model surfaces under ultra-high vacuum conditions to a broader understanding of high surface area metal nanoparticle catalysts under reaction conditions.

Results and Discussion

Computational WO_x/Pt Model and DFT Analysis

To theoretically assess the organization and structure of sub-monolayer domains of WO_x on Pt surfaces, a W_3O_7 trimer model was considered on a range of Pt surfaces, as shown in Figure 1a. The structure of W_3O_7 was studied on Pt(553), Pt(221), and kink-Pt(221) surfaces. These model surfaces exhibit two distinct classes of Pt sites across the step edge, as defined by their coordination to other Pt atoms, well-coordinated (WC, ≥ 8 nearest Pt neighbors) and under-coordinated sites (UC, ≤ 7 nearest Pt neighbors)²⁷. The influence of different metal site coordination on W_3O_7 stability is of interest considering that the surface coordination of metal nanoparticles depends on factors such as nanoparticle shape and size (Figure S1). The two different step models, Pt(221) and Pt(553), are chosen to understand the effect of terrace width on WO_x stability. Based on a recent phase diagram analysis of WO_x domains on Pt(111)²⁸, W_3O_7 is considered a representative model structure for reduced WO_x growth on metal surfaces^{15,29}. Additional WO_x models, including domains containing Brønsted acid sites (e.g., W_3O_xH), higher W oxidation states, and select W_4O_x structures were considered. These structures exhibited consistent trends in WO_x growth and organization as observed for W_3O_7 , and thus, we focus on W_3O_7 on Pt surfaces, though experimental systems likely exhibit a range of WO_x structures (see Figures S2-S3). A modified SurfGraph algorithm was utilized to estimate all possible (~ 1000) unique configurations of W_3O_7 on the Pt step model surfaces^{30–32}, as summarized in Figure 1a. The number of configurations is dictated by the different coordination numbers of the surface Pt atom(s) for a given surface model, and the orientation and structure of the adsorbed W_3O_7 trimer (Figure S4). The framework utilized to generate structures is discussed elsewhere^{32,33}, and its adaptation is detailed in the methods section.

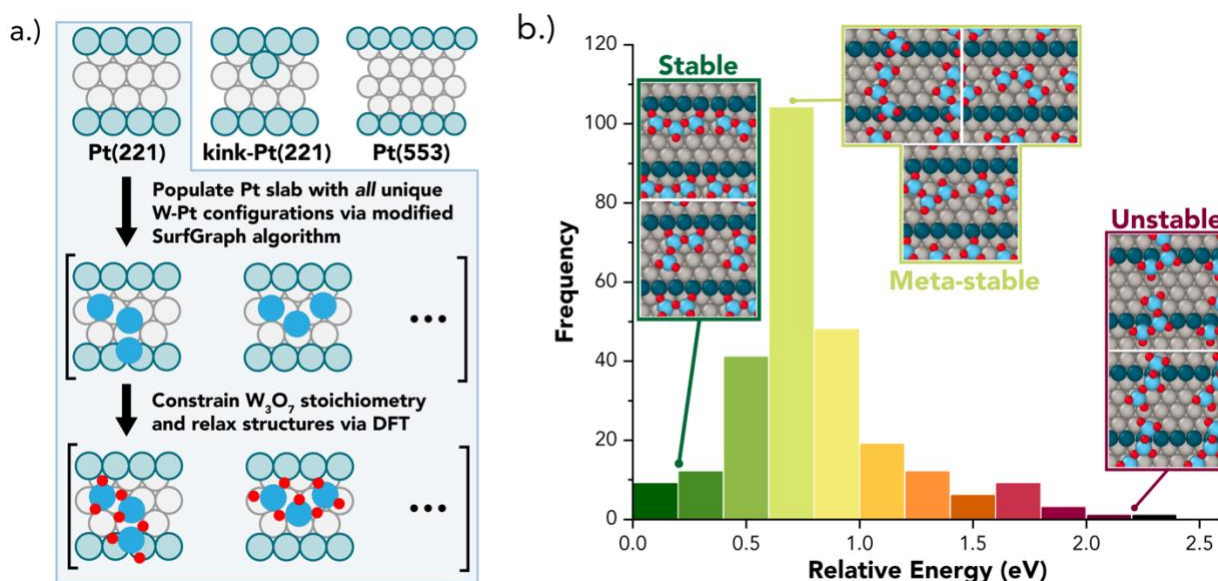


Figure 1: WO_x models on Pt step surfaces. a.) Summary of computational methods used to populate the W₃O₇ trimer model on Pt(221), kink-Pt(221), and Pt(553) surfaces, resulting in 340, 471, and 265 unique structures, respectively. b.) Histogram of DFT energies on Pt(553), with representative stable, meta-stable, and unstable structures (shown in insets). Legend: Pt_{wc} (grey), Pt_{uc} (dark blue), W (light blue), O (red)

DFT calculations were performed on the enumerated configurations to assess the stability of the SurfGraph-generated structures. As a representative case, the formation energy relative to the most stable W₃O₇/Pt structure is plotted as a histogram for various W₃O₇ structures on Pt(553) in Figure 1b. The most stable W₃O₇ structures (green bars in Figure 1b) preferentially adsorb on Pt_{wc} sites on the terrace adjacent to the Pt step edge, enabling a bond between O of WO_x and Pt_{uc} sites at the step edge. The distances between W in adjacent periodic images is at least 4.75 Å, suggesting minimal interaction and influence of computation cell size (Figure S5). Interaction between O and Pt_{uc} sites is typically more favorable than interaction with WC Pt sites by 0.2-0.3 eV, hence predicting WO_x growth initiating at step edges^{34,35}. Projected DOS for W₃O₇/Pt(553) exhibits features between WO₃ and WO₂, suggesting W oxidation states including W⁴⁺, W⁵⁺, and W⁶⁺ (Figure S6). The meta-stable structures (yellow bars), which are 0.5–1 eV uphill compared to the most stable ones, contain W mostly on the terrace with fewer W-O-Pt_{uc} bonds. Further, structures with direct W-Pt_{uc} interactions are > 0.6 eV higher in energy than the most stable structure. The most unstable structures (red bars), > 1 eV higher in energy than the most stable structures, contain multiple W bonding directly to Pt_{uc} sites or WO_x oriented across the step edge. Applying a Boltzmann distribution to the Pt(553) structure histogram in Figure 1, practically, only structures within 0.1 eV of the most stable structure will be accessible (Figure S7) under relevant conditions assuming the facile surface diffusion of oxide oligomers on metals^{20,36}. While Pt(553) provides insight into the structural motifs of WO_x organization on the Pt surface, machine learning modeling was also employed to identify the dominant features that dictate W₃O₇ stability.

Characteristic Features via Machine-Learning

The DFT calculated energetics and structures for WO_x/Pt configurations on all three Pt model surfaces were combined into a single dataset. Ten geometric features, shown in Table 1 below,

were calculated for each configuration to train a machine learning model (XGBoost) against the respective DFT energy^{37,38}.

Table 1

	Name	Range	# of Values
Z-Height above Pt surface for each W atom in W ₃ O ₇	Z _{w#}	1-3 Å	3
Coordination number of Pt for each Pt-W bond	CN _{w#}	7-10	3
Pt-O Bonds	Pt-O	0-2	1
Z-Height of W-O-W pairs grouped by bond angle	ΔZ _#	1-3 Å	2
W-O-W bond angles	θ _{wow}	120°-170°	1
Total Features			10

Table 1: Features and parameter ranges used in the XGBoost modelling of WO_x/Pt(553) structures.

These features include: (i) (3) Z-heights for each of the three W atoms of the trimer with respect to the last row of Pt-terrace atoms, (ii) (3) average coordination numbers of the Pt atom(s) bound to each of the three W atoms, (iii) the number of O-Pt_{UC} bonds, (iv) (2) Z-heights of the W atoms in the W-O-W pair with the largest W-O-W angle, and (v) the largest W-O-W angle. These are intuitive geometric parameters and provide a basis for a model to understand W₃O₇ stability on Pt surfaces. W atoms were assigned an identifier (eg. W1, W2, W3), universal to all structures, based on their Z-height per feature (i) above. A 65:35 training:test split was utilized on the 1,023 configurations. Figure 2a-b shows the model training and testing. The black dashed lines represent the parity line and the red dashed lines represent bounds of a width of 0.25 eV. A mean absolute error (MAE) of 0.14 eV was estimated, and the majority of the 358 testing points (81.6%) were inside the bounds. Utilizing the surrogate model, the gain metric was used to estimate the features contributing the most to the model fitting and were plotted in Figure 2c³⁹.

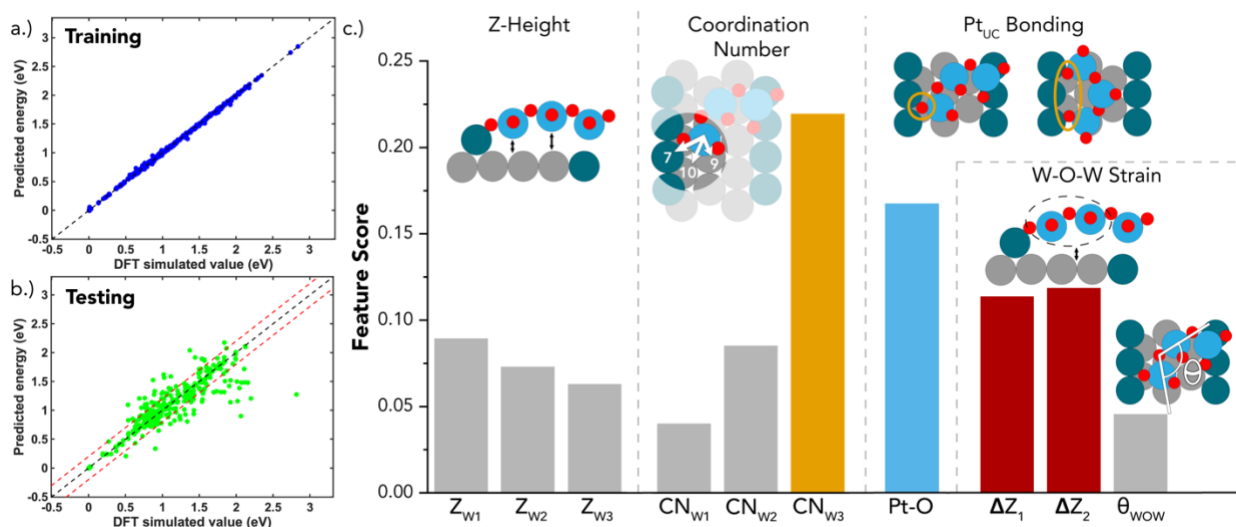


Figure 2: XGBoost model predicting dominant geometric features driving stability of WO_x on Pt(553) surfaces. a-b.) Training plot and parity plot of 65:35 split in model development. c.) XGBoost derived feature score for each feature trained in the ML model, with dominant features (CN_{w3}, Pt-O, and ΔZ_{1,2}) highlighted in color.

The three most important features are: (i) the coordination number of the Pt sites onto which the W atoms with the lowest Z-height are adsorbed, (ii) the presence of O-Pt_{UC} bond(s), and (iii) the Z-height of the W atoms with the largest W-O-W bond angle. Features (i) and (ii) together showcase the stability of W atoms on Pt_{WC} sites in the concave region close to the Pt step edge that maximize the interaction of O with Pt_{UC} sites, while avoiding direct interaction of W with Pt_{UC}. Every O-Pt_{UC} bond stabilizes the W₃O₇ structure by ~0.2 eV compared to Pt(111), in agreement with the values of O bonding to Pt_{UC} sites in surface science^{34,35}. However, the maximum number of Pt-O-W bonds formed by each W₃O₇ trimer is limited due to the lattice mismatch between Pt and WO_x. The Pt-Pt bonds have a bond distance of 2.8 Å^{40,41}, while the W-W bond length in WO_x is ~ 3.3 Å⁴²⁻⁴⁴, resulting in a buckled garland-like W₃O₇ structure along the step edge (see most stable structure in Figure 1b). The importance of this “garland-like” structure toward the accessibility of undercoordinated Pt sites to adsorbates is discussed later. Feature (iii) highlights the role of strain in W-O-W bonds in stabilizing WO_x on Pt. Structures with large W-O-W angles, arising from one W atom present on top of a Pt_{UC} site and the other in the concave region (shown in Figure 1b as unstable structures), are less stable compared to ones with a smaller W-O-W bond angle (Figure 1b stable structures). However, intuiting the effect of W-O-W bond angle on the formation energy of WO_x is challenging to do manually and showcases the ability of ML-based methods to provide physical insights from complex configurational datasets.

The analysis highlights the importance of both step edges along with terrace sites in driving the stability of WO_x on Pt. The analysis predicts Pt_{WC} sites preferentially being decorated by WO_x on the terraces of Pt nanoparticles, with Pt_{UC} sites being only partially decorated by interacting with and anchoring the O of WO_x.

Heterogeneous WO_x/Pt/SiO₂ Catalyst Characterization

To analyze the computationally predicted, site-dependent decoration of WO_x on stepped Pt surfaces, heterogeneous inverse WO_x/Pt/SiO₂ catalysts were synthesized. A Pt/SiO₂ catalyst was prepared via a modified strong electrostatic adsorption (SEA) procedure at 6% Pt weight loading⁴⁵⁻⁴⁷. SiO₂ was chosen as the catalyst support material due to its inactivity in HDO^{48,49}, low acidity, irreducibility, and amenability for spectroscopic characterization (e.g. compared to C supports which are often used in HDO but are black and thus are not conducive to UV-Vis-IR spectroscopy). Pt/SiO₂ catalysts exhibited an average Pt particle diameter of 11 ± 6 nm as measured by HAADF-STEM (Figure S8). This particle diameter was intentionally selected to align with the metal particle sizes of inverse oxide-on-metal materials previously studied in literature that exhibited notable performance in HDO of phenolics^{16,17}. Additionally, no clusters or single atom Pt species could be identified by HAADF-STEM, nor any other characterization technique employed and discussed later, highlighting that all Pt-based reactivity can be attributed to nanoparticles.

WO_x was deposited via wet impregnation of the Pt/SiO₂ catalysts using an aqueous solution of ammonium metatungstate, (NH₄)₆H₂W₁₂O₄₀, with W weight loadings varied from 0.1-6 wt%. For simplicity, WO_x-loaded Pt/SiO₂ catalysts will be referred to as xW6Pt, where x is equal to the weight loading of W. Stepwise preparation of WO_x/Pt/SiO₂ catalysts enabled the development of catalysts with varying W loading and consistent Pt particle size distributions, which was essential to determine the role of WO_x overcoating of Pt on catalyst performance. HAADF-STEM images collected of 0.1W6Pt indicate that the average Pt particle size remains unchanged after WO_x

deposition steps (Figure S9-10). This synthesis procedure differs from inverse catalysts prepared via atomic layer deposition in that, here, WO_x is deposited uniformly over the surface of the SiO_2 catalyst, without preferential deposition on Pt nanoparticle surfaces. HAADF-STEM imaging of as-prepared 6W6Pt (Figure S11) shows that WO_x is observed both as isolated monomeric W species on SiO_2 , as well as densely-packed WO_x oligomers that form 2D, film-like domains on the SiO_2 support. This is consistent with prior work that suggests that WO_x wets the surfaces of transition metal oxides and preferentially forms a monolayer-like structure before aggregation into well-ordered, 3D WO_3 particles^{50,51}. The structures observed in HAADF-STEM are also consistent with UV-VIS measurements of the as-prepared $\text{WO}_x/\text{Pt}/\text{SiO}_2$, which exhibit edge energy consistent with the existence of monomeric and polymeric WO_x species (Figure S12).

HAADF-STEM imaging of 6W6Pt shows no evidence of WO_x decoration on Pt surfaces in the as-prepared materials following calcination in oxygen that is required to form WO_x from the precursor (Figure 3a). This demonstrates that under the oxidative conditions of catalyst synthesis (i.e. calcination), WO_x domains deposit on the SiO_2 support rather than the Pt surface. This is either due to the significantly higher surface area of the SiO_2 support, or the instability of WO_x decoration on Pt when the Pt surface is oxidized and the WO_x is in its highest oxidation state (likely W^{6+}).

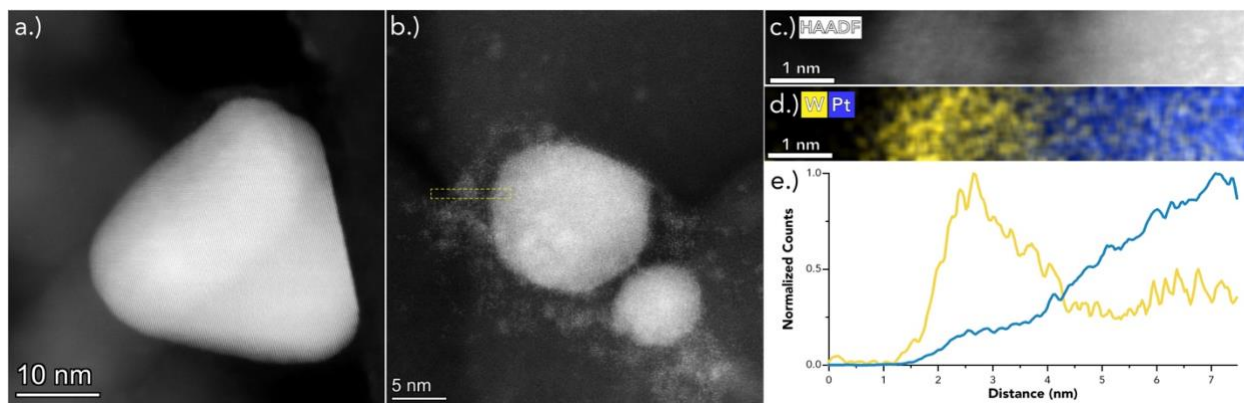


Figure 3: HAADF-STEM images of 6% W/6% Pt/ SiO_2 catalyst a.) before and b.) after reduction at 325°C for 1 hour in 10% H_2/Ar . c-e.) EDS map of the selected area in b.) shown by the yellow dashed box. EDS map evidences close spatial interaction between a W-rich layer (WO_x) and a Pt-rich area at the interface of a Pt nanoparticle seen in HAADF-STEM.

To explore the response of catalyst structure to reducing conditions, the as-prepared 6W6Pt was reduced in 10% H_2/Ar at 325°C for 1 hour and then analyzed *ex-situ* by HAADF-STEM. Air contact between treatment and imaging was minimized by transporting the sample in an Ar-flushed vial. HAADF-STEM images, shown in Figure 3b and Figure S13, indicate noticeable changes to the surfaces of Pt nanoparticles induced by H_2 reduction, wherein visible overcoating exists on the surfaces of Pt nanoparticles. These overlayers both exist as disordered domains surrounding Pt nanoparticles and more ordered overlayers of uniform thickness. We attribute the differences in these two classes of overlayers to the degree of oxidation experienced in sample transfer between the reductive pre-treatment and the microscope. Beam effects have been excluded as the cause of these overcoating structures on Pt nanoparticles considering the absence of overlayers in as-prepared $\text{WO}_x/\text{Pt}/\text{SiO}_2$ materials following calcination, as well as the use of low beam currents during STEM imaging (<20 pA).

To confirm the composition of the overlayer observed in *ex-situ* imaging of reduced 6W6Pt, EDS was performed (Figure 3c-e). EDS demonstrates the presence of W and Pt in close proximity at the outer edge of the imaged particle (Figure 3d), suggesting that the W has decorated the Pt particle. The region imaged in EDS exists over a gap in the sample and substrate, supporting that W is bound to the Pt surface and not on the SiO₂ support existing below the edge of the Pt nanoparticle. Integration of the EDS results (Figure 3d) shows that the W signal increases along with Pt signal, also supporting the close interaction of these two domains. The peak maximum of W signal prior to the significant increase of Pt signal, which remains high over the region of the nanoparticle itself, highlights that the overlayer is likely entirely composed of W, and not a combination of W and Pt, such as in an alloy phase which has been previously identified for W/Ni catalysts⁵². Thus, *ex-situ* HAADF-STEM results identify that WO_x overlayers form on Pt particles during reductive pre-treatments via WO_x mobilization from the SiO₂ support to the Pt surface. However, further structural information as to the dynamics, extent, and structure of WO_x decoration cannot be assessed via STEM alone due to the use of *ex-situ* measurements and the lack of statistically relevant sampling.

To explore the dynamic behavior of the catalyst structure and oxidation state under *in-situ* conditions, UV-Vis and CO probe molecule diffuse reflectance infrared spectroscopy (DRIFTS) were performed. UV-Vis provides information on the oxidation state of W species and CO DRIFTS probes the nature and quantity of exposed Pt sites. Various pre-treatments were studied. 6W6Pt was first oxidized to investigate the dehydrated, as-prepared state of the catalyst. Then, 6W6Pt was reduced at 225 °C in the presence of 10% CO/Ar. CO is a mild reductant that does not reduce WO_x domains under the conditions studied here⁵³ (Figure S14). However, CO does readily reduce PtO_x through CO oxidation to CO₂, thus allowing the characterization of the catalyst with Pt in the metallic state and WO_x in the fully oxidized +6 state⁵⁴. This pre-treatment was important in the comparison of WO_x/Pt/SiO₂ catalysts with Pt/SiO₂, as the reductive H₂ pre-treatments typically used in the characterization of Pt/SiO₂ catalysts would have resulted in the formation of WO_x overlayers on Pt in WO_x/Pt/SiO₂. After CO treatment, 6W6Pt was then reduced under 10% H₂/Ar, as in the HAADF-STEM experiments. Finally, the reversibility of observed changes was explored by conducting a second oxidation step. With the exception of the so-called oxidative SMSI state⁵⁵⁻⁵⁷, wherein catalyst overlayers remain stable under O₂ atmospheres (typically at elevated temperatures), oxidation is expected to return the catalyst to the initial state exhibiting oxidized WO_x domains on SiO₂ and no WO_x coverage of Pt^{1,2}.

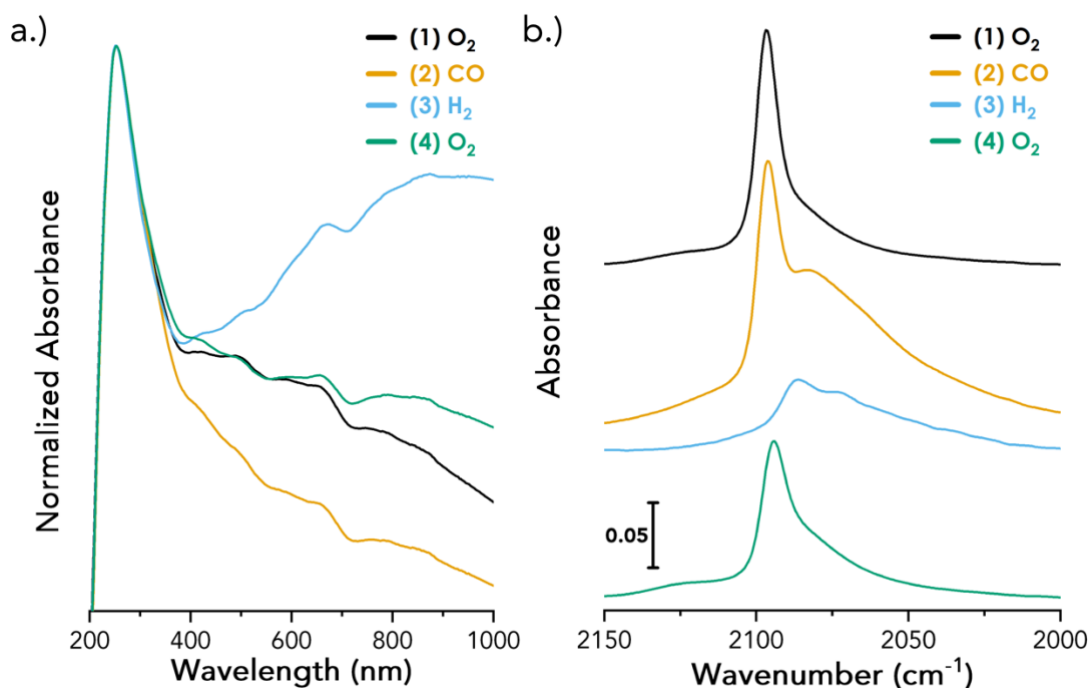


Figure 4: a.) UV-Vis and b.) CO DRIFTS spectra of 6W6Pt. Spectra collected under Ar flow at 30°C after the pre-treatment step listed. Oxidations performed at 400°C for 1 hour under UHP O₂. CO reduction conducted at 225°C for 1 hour under 10% CO/Ar. H₂ reduction performed at 325°C for 1 hour under 10% H₂/Ar.

Figure 4a shows the UV-Vis spectra of 6W6Pt collected under Ar at room temperature after the pre-treatment sequence described above. All spectra exhibit absorbance around 250 nm, which is related to the ligand-to-metal charge transfer (LMCT) between W and O associated with W⁶⁺ in WO₃ domains⁵⁰. After the initial oxidation step, this is the only feature visible in the UV-Vis spectrum. The spectrum collected after CO pre-treatment shows no additional features other than a shift in the baseline at wavelengths between 400-1000 nm, which is related to changes in the overall optical properties of the material. This is likely caused by PtO_x reduction to a metallic Pt phase⁵⁸. After H₂ treatment, a strong, broad feature is observed between 600-1000 nm, assigned to reduced W⁴⁺ and W⁵⁺ states, centered at ~500 nm and ~800 nm, respectively, that form from the WO₃ reduction^{59,60}. Recent work has suggested that the absorption stems from intervalence charge transfer (IVCT) of mixed valent W-O-W pairs (e.g. W⁵⁺-O-W⁶⁺)^{61,62}. Deconvolution of this broad absorbance is suggestive of the presence of predominantly W⁵⁺ species after this step (Figure S15), though the relative cross-sections of these two absorption bands have not been reported, preventing confident quantification of the two species through UV-Vis. The second oxidation step eliminates this feature, and the sample absorption spectrum becomes essentially identical to the initial spectrum assigned to W⁶⁺, highlighting the reversibility of oxidation state changes for W in this catalyst.

To complement the HAADF-STEM results, which identified macroscopic changes to the organization and location of WO_x in response to reduction, and UV-Vis, which provided information into the oxidation state of W species, CO DRIFTS was performed. CO DRIFTS provides insights into the accessibility, geometric, and electronic state of Pt surface sites by probing the vibrational frequency of bound CO⁶³⁻⁶⁵. Considering the DFT calculations that identified

preferential site decoration by WO_x on the terrace regions of Pt, insights into the nature of exposed Pt sites are essential to understand the location of WO_x overlayers on Pt surfaces, particularly for sub-monolayer coverages.

CO DRIFTS spectra were collected for 6W6Pt following each of the treatments previously discussed in the UV-Vis characterization. After each treatment, the sample was cooled to room temperature, exposed to CO until saturation coverage was reached, and then the cell was purged of CO by flowing Ar. Overall, the CO DRIFTS spectra (Figure 4b) show similar trends to the UV-Vis results in regard to overall reversibility of WO_x decoration of Pt nanoparticles. After the initial oxidative pre-treatment, a single main feature is observed centered at 2096 cm^{-1} , corresponding to CO bound linearly to WC Pt sites located on low-index terraces such as Pt(111) and Pt(100) surfaces^{27,66,67}. Additionally, a small, broad shoulder exists around 2120 cm^{-1} , assigned to CO bound to cationic Pt species, likely stemming from PtO_x clusters or oxidized surface Pt species^{68,69}. Since the catalyst has not been reduced prior to CO exposure in this step of the experiment, Pt surfaces are expected to exhibit high O coverage, which can inhibit or co-exist with CO bound on the surface^{70,71}. CO adsorption on WC metallic Pt sites is visible in this spectrum due to the CO oxidation reaction, which can consume surface oxygen (even at 30°C) leaving metallic Pt sites available for CO adsorption^{54,70}. This contrasts UC sites, found at steps, edges, and other defects on the Pt surface, which exhibit higher O binding energies^{72,73} and are not considered active for CO oxidation under these conditions^{74,75}.

This conclusion is supported by the spectrum collected for 6W6Pt after reduction in a CO atmosphere at 225°C in the following step. The resulting spectrum is characterized by two strong features, the same WC site feature at 2096 cm^{-1} as seen after oxidation and a second, newly exposed feature at 2080 cm^{-1} , assigned to CO bound to metallic UC Pt sites^{27,76}. Exposing the catalyst to CO at 225°C enables the CO oxidation reaction to occur on both WC and UC sites, consuming Pt-bound surface O species without reducing or otherwise mobilizing WO_x as shown in the UV-Vis results. The resulting spectrum, exhibiting the WC and UC features, is nearly identical to the CO-DRIFTS spectrum of the Pt/SiO₂ taken after reduction in H₂ (Figure 5a), supporting the conclusion that this spectrum is representative of a reduced Pt surface that is not overcoated by WO_x . Additionally, the similarity between CO-reduced 6W6Pt and H₂-reduced Pt/SiO₂ is further evidence that the WO_x deposition steps do not appreciably change the characteristics of the Pt nanoparticles, thus enabling direct comparison of the WO_x -modified catalysts with the unmodified catalyst. A small shoulder still persists at 2120 cm^{-1} , indicating that a small fraction of PtO_x domains present after oxidation were not reduced by the 10% CO/Ar atmosphere at 225°C . Indeed, it has been previously shown that small PtO_x clusters can be difficult to reduce, even under H₂ atmosphere⁷⁷.

The CO DRIFT spectrum of 6W6Pt changes in shape and intensity after H₂ treatment and CO re-adsorption to saturation coverage at 30°C . The loss of adsorbed CO intensity after H₂ treatment is consistent with the loss of Pt sites available to adsorb CO due to reduced WO_x overlayer formation, which were evidenced by UV-Vis based on W^{4+} and W^{5+} formation and seen in HAADF-STEM images. The CO stretching band is characterized by two convoluted features centered at 2085 and 2072 cm^{-1} , which are assigned to CO bound to WC and UC Pt sites, respectively, that remain after WO_x migration onto Pt. The relative intensities of the two features have changed after H₂ reduction, as compared to CO reduction, and the peak centers have shifted. These two observations

provide important information about the state of WO_x decoration on the Pt surface and will be discussed in more detail below.

Following re-oxidation and re-adsorption of CO to saturation coverage at 30°C , a similar spectrum is observed for 6W6Pt as compared to the initial oxidation, characterized by a single strong feature at 2095 cm^{-1} and a shoulder at 2120 cm^{-1} . These two features are assigned to CO bound linearly to WC Pt sites and CO bound to cationic Pt species in PtO_x domains, as previously discussed. The similarity of the CO DRIFTS spectrum following the first and last oxidation steps is evidence that, in addition to the reversibility of WO_x reduction evidenced by UV-Vis spectroscopy, the decoration of the Pt surface by WO_x is reversible in response to the pre-treatment atmosphere used.

For 6W6Pt, the molar ratio of W:Pt is approximately 1, though there is a considerable excess of W compared to the number of surface Pt sites when accounting for the low dispersion of the $\sim 10\text{ nm}$ Pt nanoparticles present in the Pt/SiO₂ catalyst. Thus, under reducing conditions, a large fraction of the Pt sites could be decorated by the reduced WO_x overlayer, as evidenced by the drop in the peak area associated with adsorbed CO species in the CO DRIFTS spectrum after H₂ reduction (Figure 4b). As alluded to previously, however, the relative peak areas associated with CO adsorption on WC and UC sites changed between CO and H₂ pre-treatments. Specifically, peak area associated with CO on WC Pt sites apparently decreased more than the peak area associated with CO adsorption on UC sites, suggesting that reduced WO_x species more effectively decorated WC sites than UC sites. This trend is opposite what would be expected even when taking relative extinction coefficients of CO bound to WC and UC sites into account, since perfectly non-preferential decoration would result in greater loss of UC site area relative to WC site area due to the higher extinction coefficient of UC sites^{64,78}.

To explore this in more depth, a series of WO_x -modified catalysts were synthesized from the same Pt/SiO₂ catalyst in the range of 0-6 wt% W. Moderation of W loading enabled control over the amount of WO_x overlayer formation on the Pt surface after H₂ reduction. CO DRIFT spectra of the $\text{WO}_x/\text{Pt}/\text{SiO}_2$ materials with varying W loading following H₂ reduction are shown in Figure 5a. As discussed previously, the CO probe molecule DRIFT spectrum of the 6% Pt/SiO₂ catalyst without WO_x modification following H₂ reduction is qualitatively similar to the CO-reduced $\text{WO}_x/\text{Pt}/\text{SiO}_2$ shown in Figure 4b, exhibiting CO adsorption on both WC and UC features at 2087 and 2050 cm^{-1} , respectively. The relative peak areas and centers differ slightly for the spectrum shown in Figure 5a compared to that shown in Figure 4b due to differences in pre-treatment conditions between the two spectra.

Strikingly, CO DRIFT spectra of materials with increasing WO_x loadings following H₂ reduction exhibit a loss of intensity of the feature associated with CO adsorption on WC Pt sites, while the feature associated with CO adsorption on UC Pt sites exhibits comparatively less change. This is consistent with the preferential decoration of WC Pt sites by WO_x following H₂ reduction. Spectral deconvolution was performed using 4 Gaussian peaks, with 2 peaks being used for both the CO adsorption on WC and UC Pt sites to capture inherent peak asymmetry⁶³ and heterogeneity introduced by partial WO_x decoration on the Pt surface (Figure 5b). Deconvolution results for all materials and parameters can be found in Figure S16 and Table S1, respectively. As introduced briefly above, the molar extinction coefficient of CO bound to UC Pt sites has been reported to be 2.7 greater than the molar extinction coefficient of CO bound to WC Pt sites^{64,78}. The relative molar

extinction coefficient was used to determine the fraction of adsorbed CO residing on WC and UC Pt for each $\text{WO}_x/\text{Pt}/\text{SiO}_2$ catalyst following H_2 reduction. Figure 5c shows that there is a monotonic, linear loss in the fraction of WC sites relative to UC sites as a function of W loading, demonstrating the preferential decoration of WC sites on the Pt surface by WO_x after H_2 reduction.

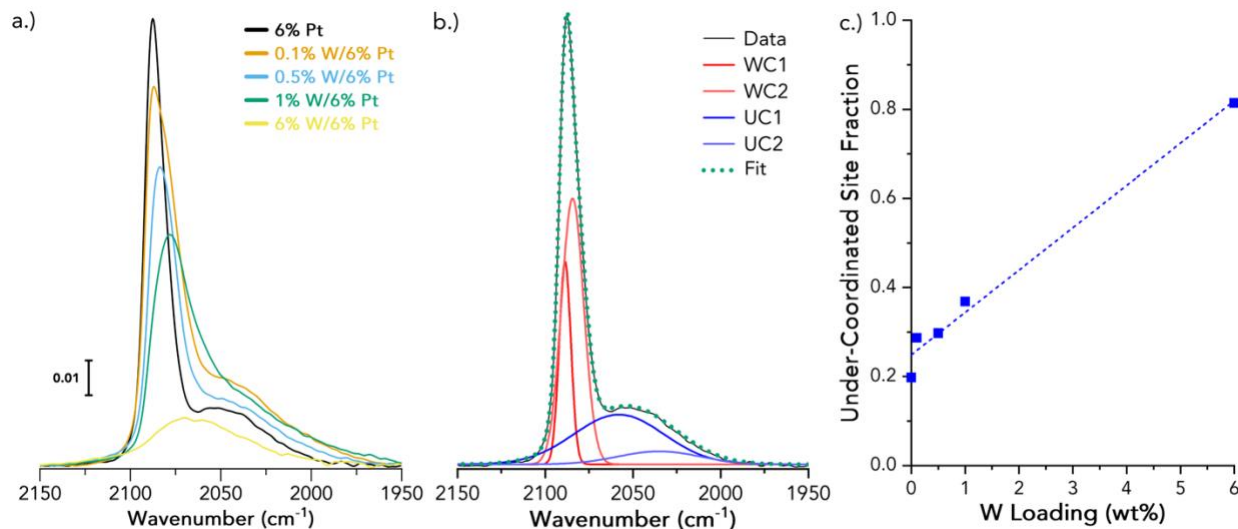


Figure 5: a.) CO DRIFTS spectra of various W loadings on 6% Pt/SiO₂. Spectra were collected at 30°C. Catalysts were first oxidized at 400°C for 1 hour in UHP O₂ before reduction in 10% H₂/Ar at 325°C for 1 hour. CO adsorption conducted at 30°C for 15 minutes before purging gas-phase CO from the cell with Ar. b.) Gaussian deconvolution of 6% Pt/SiO₂ using 4 features, 2 for each WC and UC feature. c.) UC site fraction determined by Gaussian fits of each $\text{WO}_x/\text{Pt}/\text{SiO}_2$ catalyst.

In addition to changes in the relative peak areas associated with the WC and UC Pt sites with increasing WO_x loading, there are also changes to peak centers in the CO DRIFTS spectra. The peak associated with CO bound linearly to WC Pt sites red-shifts to lower wavenumbers, whereas CO bound linearly to UC Pt sites blue-shifts to higher wavenumbers. The red-shifting of the WC feature is assigned to decreased dipole-dipole coupling on Pt terraces due to the presence of WO_x on these sites, consistent with WO_x localizing on WC Pt terraces. Dipole-dipole coupling for CO on extended metallic surfaces occurs when low energy modes transfer energy to higher energy states, resulting in the observed blue-shift to CO vibrational frequency with increasing CO coverage on extended surfaces. When this coupling is disrupted, as we propose is the case in WO_x decoration, the CO stretch red-shifts. Analogous shifts have been observed for both alloyed materials (CuPt) and isotopic exchange experiments between ¹²CO and ¹³CO, which don't vibrationally couple, highlighting that decreased effective CO coverage on WC sites caused by WO_x addition results in a red-shift the CO stretching frequency⁷⁹. On the other hand, the blue-shift of the feature associated with CO adsorption on Pt UC sites (Figure S17) cannot be ascribed to decreased CO coverage. In general, CO bound to UC sites exhibit less significant dipole-dipole coupling than on extended surfaces due to the spatial separation of adsorbates on stepped surfaces, reducing their ability to electronically couple⁸⁰. Instead, the blue-shift of the UC feature is attributed to electronic modification of UC Pt sites by proximal WO_x units. A Pt/ WO_3 catalyst

synthesized for comparison demonstrates that Pt sites near WO_x are blue-shifted compared to their Pt/SiO₂ analogues due to this electronic (charge transfer) effect (Figure S18).

The suspected electronic interaction of WO_x with UC Pt sites can be further understood by modelling CO adsorption for the most stable $\text{W}_3\text{O}_7/\text{Pt}(553)$ model and a pure Pt(553) surface, as shown in Figure 6a. The SurfGraph algorithm was used to populate all unique configurations of CO in the presence and absence of W_3O_7 , and UC Pt sites were predicted to be the most thermodynamically favorable CO adsorption sites for both surfaces, regardless of the presence of W_3O_7 . In the case of the W_3O_7 -modified Pt(553) surface, CO was most stable on the UC Pt sites between the W_3O_7 unit, essentially inside the so-called “garland” structure (Figure 6a, bottom image). Additional favorable adsorption structures can be found in Figure S19. CO binding on the UC Pt site involved in Pt-O-W bonding resulted in the breaking of the Pt-O-W bond and was less energetically favorable. As mentioned previously, the preferred garland-like structures enable UC Pt sites to continue to be accessible to adsorbates and may explain the ability of Pt- WO_x catalyst to adsorb CO on UC Pt sites at WO_x loadings greater than a monolayer equivalent, as seen for 30% W/6% Pt/SiO₂ (Figure S20). Given that the formation energy of the most stable trimer W_3O_7 structure is energetically favorable, we believe that the key features stabilizing WO_x will be similar at high W coverage as well.

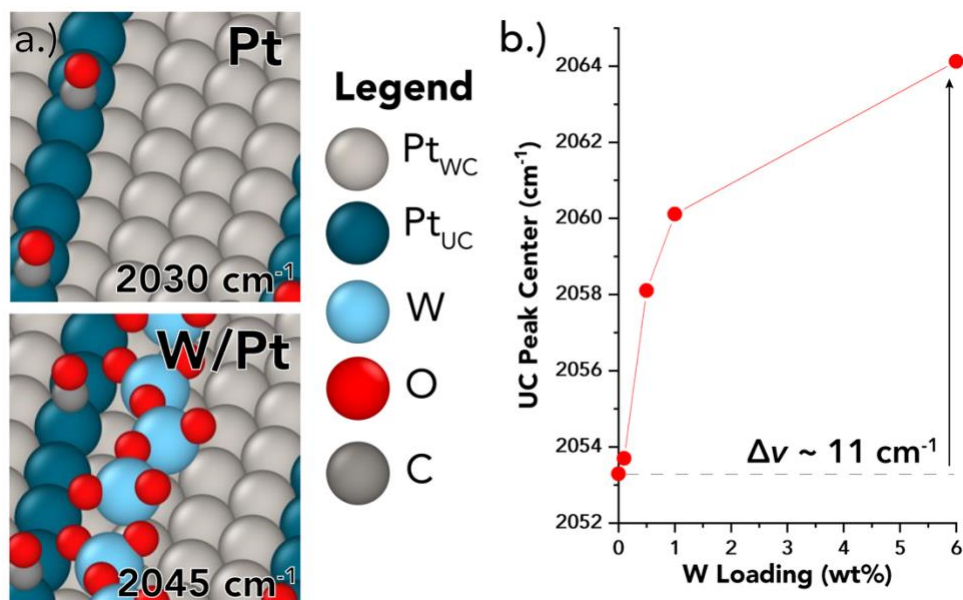


Figure 6: a.) DFT-predicted vibrational frequency shift of a single CO molecule bound to a Pt step on Pt and WO_x/Pt model surfaces. b.) Peak shift of the UC feature with increasing W loading in the CO DRIFTS spectrum determined from deconvolution. Strong agreement in the magnitude of the peak shift with experiments with increasing W loading indicates that experimental shifts are due to increasing WO_x interaction with UC Pt sites.

DFT calculations predict the most exothermic binding energy of CO^* in presence of W_3O_7 to be 0.2 eV weaker than on pure Pt, alluding to electronic modification of the Pt site due to the presence of WO_x . This electronic interaction also results in CO stretching frequencies of between 2041-2045 cm⁻¹, depending on CO coverage (Figures 6a and S21), on the most stable adsorption site for $\text{WO}_x/\text{Pt}(553)$, compared to 2030 cm⁻¹ for the same site on bare Pt(553); thus, a blue shift in the CO frequency of $\sim 15 \text{ cm}^{-1}$ due to W_3O_7 addition was observed. Figure 6b shows the analysis of the deconvoluted CO DRIFTS spectra from Figure 5, which evidence a blue-shift of the UC feature

of $\sim 11 \text{ cm}^{-1}$, consistent with the shift calculated via DFT. The discrepancy in absolute peak positions for CO bound to the UC Pt site in experiment ($\sim 2060 \text{ cm}^{-1}$) and the DFT (2045 cm^{-1}) is a common feature of DFT vibrational calculations and stems from, among others, differences in adsorbate coverages and functional choice⁸¹.

Collectively, the characterization of heterogeneous inverse $\text{WO}_x/\text{Pt}/\text{SiO}_2$ catalysts demonstrates that WO_x reduces and mobilizes under H_2 atmospheres to preferentially decorate WC sites on the surface of Pt nanoparticles. This is consistent with the DFT calculations, which concluded that WO_x growth on Pt terraces is energetically favored over WO_x growth across Pt steps. Further, the theoretical models identified the formation of Pt-O-W bonds at the Pt step as particularly stabilizing of the WO_x overlayer, which is consistent with observations made from UHV studies of oxide decoration on model metal surfaces^{22–25}.

The evidenced preferential growth of WO_x on WC Pt sites should result in modified catalytic performance, specifically for reactions that exhibit structure sensitivity. As mentioned in the introduction, we recently used unmodified Pt/SiO_2 catalysts of varying Pt nanoparticle size distributions to demonstrate that WC Pt sites are responsible for aromatic ring hydrogenation during HDO of phenolics such as dihydroeugenol (DHE)¹⁹. The results discussed above evidence that WO_x preferentially decorates these same WC Pt sites under reducing conditions similar to those experienced in HDO reactions (H_2 atmosphere, elevated temperatures). Thus, the ability of WO_x/Pt catalysts and other inverse catalyst compositions to suppress undesired hydrogenation during HDO reactions could be related to sub-monolayer WO_x overlayers blocking WC sites that are particularly active for aromatic ring hydrogenation.

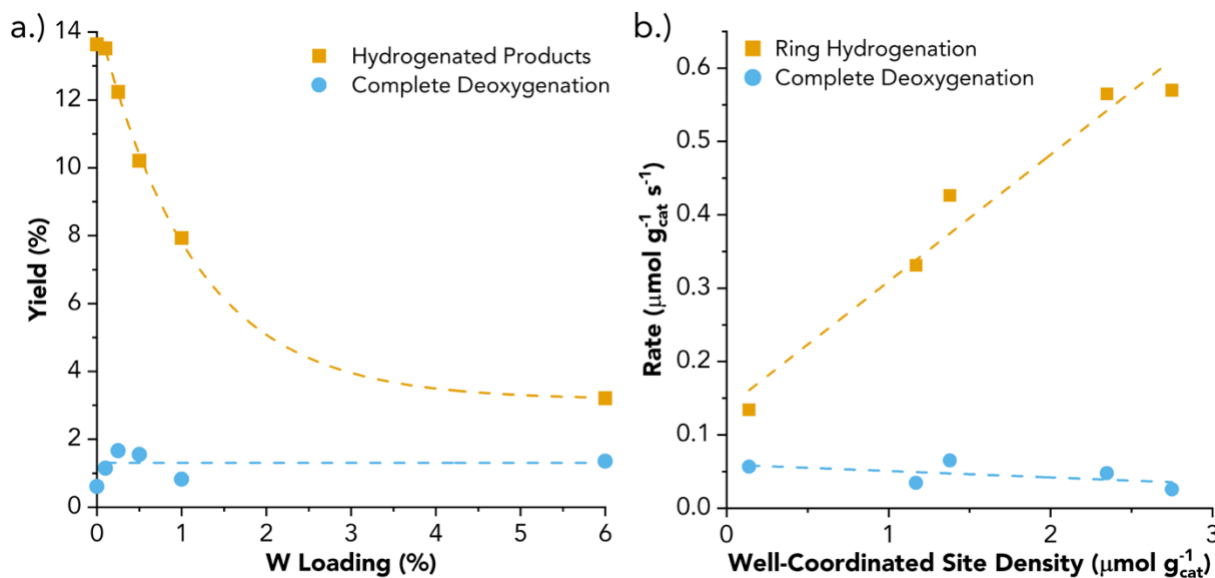


Figure 7: a.) Analysis of product yields in the HDO reaction of DHE over WO_x -modified Pt/SiO_2 catalysts. b.) Comparison of estimated hydrogenation and complete deoxygenation rates to well-coordinated site density highlights the effect of reduced well-coordinated site density on suppressed hydrogenation.

To test this hypothesis, the HDO of DHE was performed using the series of $\text{WO}_x/\text{Pt}/\text{SiO}_2$ catalysts with varying W loading. Reactions were performed in a batch reactor under magnetic stirring in the absence of mass transport limitations (S.I. Note 1). Reaction performance was normalized by loading a constant mass of Pt into the reactor for each catalyst. The products formed under reaction

conditions include those related to ring hydrogenation, such as 2-methoxy-4-propylcyclohexanol (HYD), and deoxygenation, such as 4-propylphenol (PHE) and 4-propylbenzene (BNZ), as well as the combination of the two reactions, such as 4-propylcyclohexanol (OL), 4-propylcyclohexanone (ONE), and 4-propylcyclohexane (CYC)¹⁹. HDO products were grouped into two classes, hydrogenated products (HYD, OL, ONE, CYC) and fully-deoxygenated products (CYC, BNZ).

Products and remaining substrate contributed to a mass balance after reaction of ~80%. The remaining mass is ascribed to the formation of small quantities of gas phase species, bound organics on the catalyst surface, and oligomerized products in solution, described in more detail in Figures S22-24 and Table S2⁸²⁻⁸⁵. However, control experiments indicate that oligomers and bound oxygenates are produced from DHE and not HDO products (Figure S25) – thus, the mass balance closure does not influence the measured product yields. Moreover, oligomer formation is known to occur over acid sites, such as WO_x domains, which is evidenced here by the progressive coloration of the samples with increasing WO_x loading (Figure S26). This includes WO_x domains not on Pt nanoparticles, indicating that the sites not active for HDO (i.e. WO_x/SiO₂) may be the sites most responsible for oligomer formation and organics adsorption.

The results of reactions at 275 °C for 2 hours are shown in Figure 7a, with a full list of tabulated values found in Table S2. The yield of hydrogenated products decreases with increasing W loading. This is consistent with the blockage of well-coordinated sites by WO_x, as our prior work has demonstrated that well-coordinated sites are responsible for aromatic ring hydrogenation in unmodified Pt/SiO₂ catalysts under similar conditions¹⁹. However, there is no measurable change in the yield of fully-deoxygenated products over this range of W loadings, including the case of 0% W, corresponding to the unmodified Pt/SiO₂ catalyst. It has been suggested that the role of reducible oxides modifiers, such as WO_x in HDO by Pt reactions may be to introduce oxygen vacancies that can facilitate a reverse Mars-van Krevelen-type reaction mechanism^{17,86,87}. Others have pointed to the formation of oxide-metal interfaces as an essential component of the active site structure⁸⁸⁻⁹⁰. However, the minimal change in deoxygenation activity observed here as a function of W loading suggests that WO_x is not a strong promoter of deoxygenation activity under the conditions studied; in other words, it appears from our results that the active site responsible for DHE HDO is not significantly promoted by the presence of WO_x. Instead, the trend in DHE HDO selectivity observed is suggestive of UC Pt sites, which are presumed to be accessible under reaction conditions stemming from the results of CO DRIFTS characterization, being the active site for deoxygenation. However, the influence of WO_x addition to Pt on catalyst stability and the exact identity of the active site for deoxygenation during HDO¹⁷ requires further analysis.

The impact of the preferential decoration of WC Pt sites by reduced WO_x species is further highlighted by correlating the measured rates of ring hydrogenation and complete deoxygenation against the concentration of WC sites on the catalyst surface, as shown in Figure 7b. Here, the concentration of WC sites is estimated based on the fraction of exposed Pt sites existing as WC Pt, as measured by CO DRIFTS, multiplied by the total quantity of exposed Pt sites, measured by CO chemisorption, both measured after *in situ* reduction at 325 °C in 10% H₂/Ar. It can be seen from the data spacing in Figure 7b that increasing W loading results in a consistent loss of Pt_{wc} site density. Moreover, there is no apparent relationship between the deoxygenation rate and this Pt_{wc} site density, suggesting that deoxygenation occurs on other sites on the catalyst surface, such as

UC Pt sites or interfacial sites between Pt and WO_x. As discussed above, though, it is unlikely that deoxygenation occurs over sites only consisting of WO_x, as the Pt/SiO₂ catalyst exhibits deoxygenation activity comparable to WO_x-modified catalysts. On the other hand, a monotonic, linear relationship exists between the number of WC Pt sites exposed on Pt and WO_x coated Pt surfaces and the rate of aromatic ring hydrogenation. Since Pt particle size is constant across all catalysts, this indicates that the preferential decoration of WC Pt sites by WO_x is the primary mechanism behind suppressed aromatic hydrogenation during HDO of oxygenates common to lignin monomers for inverse WO_x/Pt catalysts.

Conclusions

The structural organization of WO_x on Pt in inverse WO_x/Pt/SiO₂ catalysts exhibiting sub-monolayer WO_x overlayer coverage was investigated by theoretical and experimental approaches. DFT calculations were performed to understand the structural organization of WO_x on stepped Pt surfaces. Preferential decoration of WO_x oligomers on Pt_{WC} sites was observed with partial occupation of Pt_{UC} sites. A data-driven machine-learning algorithm identified the dominant features stabilizing WO_x as bonding between an O in WO_x and Pt_{UC} sites, the presence of W on Pt_{WC} sites adjacent to Pt_{UC} sites, and the growth of WO_x mainly on Pt_{WC} regions (terraces). An experimental system was developed using a Pt/SiO₂ catalyst modified by varying amounts of WO_x. *In-situ* spectroscopic characterization and *ex-situ* electron microscopy uncovered the dynamic reversibility of WO_x decoration of Pt surfaces, analogous to traditional SMSI catalysts, except here due to WO_x mobility to and from SiO₂. CO DRIFTS evidenced the preferential overcoating of Pt_{WC} sites with increasing WO_x loading, consistent with theoretical results. Reactivity studies in the HDO of DHE indicated that increasing WO_x loading primarily suppressed ring hydrogenation activity, with relatively little change in the yield of deoxygenated products. Considering that aromatic ring hydrogenation has been shown to occur over Pt_{WC} sites^{19,91}, our findings support that the preferential decoration of Pt_{WC} sites by WO_x identified in CO DRIFTS also occurs under reaction conditions. This work provides evidence that inverse catalysts can be designed and controlled to manipulate the number and nature of exposed metal sites, which offers a unique lever for controlling activity and selectivity in a broad range of chemistries.

Methods and Materials

DFT Evaluation of Unique WO_x/Pt Structures

The DFT simulations were performed within the framework of periodic density functional theory with the Vienna Ab Initio Simulation Package (VASP)⁹². The energies and geometries of the identified configurations of WO_x on the Pt(553) surface were obtained through minimization of the total energy with respect to geometry by generalized gradient approximation calculations (GGA-PBE)⁹³. The projected augmented wave (PAW) method was used to account for the effect of core electrons on the valence electron density⁹⁴. A PBE-calculated lattice constant of 3.98 Å for Pt bulk was employed. The Pt(553) surface was represented by a 5 × 4 unit cell with four layers (total of 56 atoms per unit cell). The Pt(221) and kink-Pt(221) surfaces were represented by a 4 × 3 unit cell with four layers (total of 33 and 34 atoms respectively). The top two layers were relaxed for all the cases and a vacuum equivalent to at least 13 Å was applied between any two successive slabs. A planewave energy cutoff of 400 eV was used for all the calculations. A minimum k-point grid sampling of 3x3x1 was employed. The electronic occupancies were determined according to a Methfessel–Paxton scheme with an energy smearing of 0.2 eV. The

cutoff for the convergence of the electronic loop (EDIFF) was set to 10^{-4} eV. Structures were fully relaxed until the Hellmann–Feynman forces acting on the atoms were smaller than 0.05 eV/Å.

XGBoost Machine Learning

The XGBoost algorithm was used³⁹. To access its robustness, different seeds were used to split the data randomly into training and testing set. Further, a 5-fold cross validation was also performed to verify the results. The XGBoost model was fit using a mean squared error loss function. Default values were utilized for the other hyperparameters. The gain metric was utilized in the feature importance calculation to estimate the features contributing the most to the model fitting.

Catalyst Synthesis

Base 6 wt% Pt/SiO₂ catalysts were synthesized via a modified strong electrostatic adsorption methodology used previously. Briefly, 2 g of spherical, non-porous SiO₂ with an average particle size of 20–30 nm (USNano) was suspended in 100 mL of deionized water (Sigma) with magnetic stirring. The suspension was adjusted to pH 10 using an appropriate amount of NH₄OH (Sigma), monitored by an electronic pH meter. After reaching pH 10 and left stirring for 10 minutes, 10 mL of a solution of tetraamine platinum nitrate (TAPN, Sigma) was added dropwise under vigorous stirring. The resulting suspension was left to stir for 30 minutes before increasing the temperature to 70°C until all the water was evaporated from the dish. The collected solids were further dried at 120°C overnight prior to calcination in a tube furnace at 600°C for 6 hours in 50 sccm dry air (Airgas).

WO_x-modified samples were prepared similarly using a wet impregnation of ammonium metatungstate (AMT, Sigma). Previously prepared 6 wt% Pt/SiO₂ was added to a dish with 20 mL of deionized water (Sigma) with magnetic stirring. To this, an appropriate amount of AMT was added to achieve the desired weight loading, in the range of 0.1 to 6 wt% by W. After stirring for 30 minutes, the solution was heated to 70°C to evaporate the water. The remaining solids were collected and dried overnight at 120°C prior to calcination in a tube furnace at 350°C for 3 hours.

Catalyst Characterization

High-annular angle dark field scanning transmission electron microscopy (HAADF-STEM) was performed on an aberration-corrected ThermoFisher Spectra 200 microscope. Typically, samples were prepared by drop casting onto a lacey carbon-coated Cu grid (400 mesh, Ted Pella). Briefly, samples were dispersed in methanol (Sigma) by physical mixing followed by sonication. 5 μL of the suspension was then dropped onto the carbon side of the grids via pipette and allowed to dry under flowing air before being placed in a vacuum oven at 100°C using house vacuum for at least 24 hours to mitigate solvent-related contamination under the electron beam. Images were collected at 200 kV. Beam current was adjusted as needed to minimize sample charging and damage, particularly in the imaging of WO_x domains which exhibited mobility on the SiO₂ support under beam illumination. Energy dispersive x-ray spectroscopy (EDS) was utilized to identify the atomic identity of Pt and W in WO_x/Pt samples due to the two elements' similar contrast in the HAADF-STEM mode.

CO DRIFTS measurements were carried out on a Nicolet iS10 FT-IR spectrometer equipped with a Praying Mantis Diffuse Reflection Accessory (Harrick Scientific) and a High-Temperature Reaction Chamber (Harrick Scientific) fitted with a thermocouple in the catalyst bed. Ar

(99.995%), He (99.995%), O₂ (99.50%), 10% CO/Ar, and 10% H₂/Ar were purchased from Airgas and used as received. In a typical DRIFTS experiment, catalyst was loaded into the Harrick cell and pre-treated under a desired gas environment and temperature. Temperature set points were reached by ramping the catalyst at 10°C/min in all experiments, except for cooling after pre-treatment steps which was allowed to happen passively. Gas flow rates across the catalyst bed in all cases was 50 sccm controlled by mass flow controllers (Teledyne Hastings). For CO DRIFTS experiments, catalysts were cooled to 30°C prior to exposure to 10% CO/Ar. CO exposure was continued until saturation coverage of CO on the metal sites was achieved, determined by unchanging peak intensity in DRIFTS spectra. After metal surfaces were saturated by CO, gas flow was switched to Ar to remove CO from the gas atmosphere. In sequential experiments, additional pre-treatments were conducted in the same manner. After each pre-treatment in the sequence, CO was re-adsorbed and purged at 30°C in the same manner. UV-Vis spectra were recorded by following an identical *in-situ* procedure to those performed during CO DRIFTS experiments, this time using a Thermo Scientific Evolution 300 spectrophotometer.

Pt site density measurements were made by performing CO pulse chemisorption using an Autochem 2920 II (Micromeritics). In a typical experiment, 50 mg of catalyst was loaded between two quartz wool plugs in a quartz cell. The catalyst was pre-treated at the desired temperature and gas atmosphere before cooling to 30°C. Pulsed measurements were made by exposing the catalyst to 10 pulses of 50 sccm 10% CO/Ar separated by 3.5 minutes of Ar flow at 50 sccm. CO uptake was measured by integrating the difference of each peak area relative to the final peak, assuming a CO:Pt ratio of 1. H₂-temperature programmed reduction (H₂-TPR) was also performed using the same instrument. Catalyst loading procedures were the same, and catalysts were typically pre-treated at 400°C for 1 hour in O₂ before being cooled to 50°C to start the TPR.

HDO Reactions

HDO reactions using the prepared catalysts were performed in 75-mL stainless-steel pressure reactors (Parr Instrument Co., 5000 Series). In a typical reaction, catalyst was loaded into the reactor along with 500 mg of dihydroeugenol (DHE, Sigma) and 20 mL of cyclohexane (Sigma). Catalyst loading was determined such that a constant mass (6 mg) of Pt was loaded for each reaction. Reactions were stirred magnetically at 700 rpm using glass-shielded stir bars. Once loaded, the reactor was sealed and purged 3 times with 5.0 grade H₂ (Airgas) before pressurizing to a final gauge pressure of 20 bar at room temperature. Then, the vessel was heated to 275 °C and held for 2 hours. After the allotted reaction time, the reactor vessel was quickly removed and quenched using a water bath. Once cooled to room temperature, the liquid products were collected by centrifugation and analyzed by a gas chromatogram equipped with a flame ionization detector (GC-FID, Agilent) using *n*-decane (Sigma) as an internal standard. Product identification was carried out using commercially-sourced standards where possible (DHE, 4-propylbenzene (BNZ), 4-propylphenol (PHE), 4-propylcyclohexanol (OL), 4-propylcyclohexane(CYC)). In instances where standards are not commercially available, FID responses were estimated using effective carbon number (ECN)⁹⁵. Reaction performance metrics were defined as:

$$\text{Conversion (\%)} = \frac{N_{DHE}}{N_{DHE}^0}$$

$$Selectivity (\%) = \frac{N_{Product}}{\sum N_{Product}}$$

$$Yield (\%) = \frac{N_{Product}}{\sum N_{Product}} * Conversion$$

where N_i is the moles of species i measured by GC-FID and N_i^0 is the initial moles of i loaded into the batch reactor.

Supporting Information

Figures S1-S26, additional HAADF-STEM images and particle size analysis, Tauc analysis of UV-Vis spectra, deconvoluted UV-Vis and CO DRIFTS spectra, additional CO DRIFTS spectra of reference catalysts, H₂-TPR analysis of 6W6Pt and 6Pt, coloration of post-HDO reaction mixtures, Boltzmann distribution of example DFT structures, additional stable CO adsorption sites for DFT models, most stable DFT structures for W₃O_xH_y stoichiometries. Tables S1-S4, tabulated parameters for CO DRIFTS deconvolution, evaluation of organics adsorption on spent catalyst, tabulated HDO reaction performance, XYZ-data for most stable W₃O₇/Pt(553) model.

Acknowledgements

This work was supported by the Catalysis Center for Energy Innovation, an Energy Frontier Research Center funded by the U.S. Department of Energy, Office of Science, Office of Basic Energy Sciences under Award No. DE-SC0001004. Electron microscopy was performed at the MRL Shared Experimental Facilities, which are supported by the MRSEC Program of the NSF under Award No. DMR 1720256; a member of the NSF-funded Materials Research Facilities Network (www.mrfn.org). P.C. and M.A.O. both acknowledge the Mellichamp Academic Initiative in Sustainability at UCSB for support.

References

1. Tauster, S. J., Fung, S. C. & Garten, R. L. Strong Metal-Support Interactions. Group 8 Noble Metals Supported on TiO₂. *J Am Chem Soc* **100**, 170–175 (1978).
2. Tauster, S. J., Fung, S. C., Baker, R. T. K. & Horsley, J. A. Strong Interactions in Supported-Metal Catalysts. *Science* (1979) **211**, 1121–1125 (1981).
3. Kliewer, C. E., Miseo, S., Baumgartner, J. E., Stach, E. & Zakharov, D. Early stage strong metal support interaction (SMSI) effects in an experimental titania-supported platinum catalyst an environmental TEM study. *Microscopy and Microanalysis* **15**, 1066–1067 (2009).
4. Matsubu, J. C. *et al.* Adsorbate-mediated strong metal-support interactions in oxide-supported Rh catalysts. *Nat Chem* **9**, 120–127 (2017).
5. Matsumoto, T., Batzill, M., Hsieh, S. & Koel, B. E. Fundamental studies of titanium oxide-Pt(100) interfaces II. Influence of oxidation and reduction reactions on the surface structure of TiO_x films on Pt(100). *Surf Sci* **572**, 146–161 (2004).
6. Hernández Mejía, C., van Deelen, T. W. & de Jong, K. P. Activity enhancement of cobalt catalysts by tuning metal-support interactions. *Nat Commun* **9**, 1–8 (2018).

7. Zhang, S. *et al.* Dynamical observation and detailed description of catalysts under strong metal-support interaction. *Nano Lett* **16**, 4528–4534 (2016).
8. Seo, H. O. *et al.* Carbon dioxide reforming of methane to synthesis gas over a TiO₂-Ni inverse catalyst. *Appl Catal A Gen* **451**, 43–49 (2013).
9. Li, Y., Zhang, Y., Qian, K. & Huang, W. Metal-Support Interactions in Metal/Oxide Catalysts and Oxide-Metal Interactions in Oxide/Metal Inverse Catalysts. *ACS Catalysis* vol. 12 1268–1287 Preprint at <https://doi.org/10.1021/acscatal.1c04854> (2022).
10. Yang, F. *et al.* CO oxidation on inverse CeO_x/Cu(111) Catalysts: High catalytic activity and ceria-promoted dissociation of O₂. *J Am Chem Soc* **133**, 3444–3451 (2011).
11. Zhao, G. *et al.* Metal/oxide interfacial effects on the selective oxidation of primary alcohols. *Nat Commun* **8**, 1–8 (2017).
12. Fu, J. *et al.* Modulating the dynamics of Brønsted acid sites on PtWO_x inverse catalyst. *Nat Catal* **5**, 144–153 (2022).
13. Polo-Garzon, F. *et al.* In situ strong metal-support interaction (SMSI) affects catalytic alcohol conversion. *ACS Catal* **11**, 1938–1945 (2021).
14. Lin, Z. *et al.* Experimental and Theoretical Insights into the Active Sites on WO_x/Pt(111) Surfaces for Dehydrogenation and Dehydration Reactions. *ACS Catal* **11**, 8023–8032 (2021).
15. Lin, Z. *et al.* Mechanistic Understanding of Ring-Opening of Tetrahydrofurfuryl Alcohol over WO_x-Modified Pt Model Surfaces and Powder Catalysts. *ACS Catal* **13**, 8014–8024 (2023).
16. Wang, C. *et al.* Hydrodeoxygenation of m-Cresol Over Pt-WO_x/C Using H₂ Generated In Situ by n-Hexane Dehydrogenation. *Catal Letters* **150**, 913–921 (2020).
17. Wang, C. *et al.* Mechanistic Study of the Direct Hydrodeoxygenation of m-Cresol over WO_x-Decorated Pt/C Catalysts. *ACS Catal* **8**, 7749–7759 (2018).
18. Huang, R., Kwon, O., Lin, C. & Gorte, R. J. The effects of SMSI on m-Cresol hydrodeoxygenation over Pt/Nb₂O₅ and Pt/TiO₂. *J Catal* **398**, 102–108 (2021).
19. Marlowe, J., Ford, P. C., Abu-Omar, M. M. & Christopher, P. Structure sensitivity in Pt-catalyzed hydrodeoxygenation of multi-oxygenated lignol model compounds. *Catal Sci Technol* **13**, 5662–5678 (2023).
20. Lavroff, R. H., Wang, J., White, M. G., Sautet, P. & Alexandrova, A. N. Mechanism of Stoichiometrically Governed Titanium Oxide Brownian Tree Formation on Stepped Au(111). *Journal of Physical Chemistry C* **127**, 8030–8040 (2023).
21. Wang, J. *et al.* Surface structure of mass-selected niobium oxide nanoclusters on Au(111). *Nanotechnology* **32**, 1–12 (2021).
22. Li, F., Allegretti, F., Surnev, S. & Netzer, F. P. Atomic engineering of oxide nanostructure superlattices. *Surf Sci* **604**, (2010).
23. Kurzina, I. & Atrei, A. STEP REARRANGEMENT UPON LOW PRESSURE OXIDATION OF THE Pt₃Ti(510) SURFACE: A STUDY BY SCANNING TUNNELING MICROSCOPY. *Surface Review and Letters* **10**, 861–866 (2003).
24. Lu, J. *et al.* First-principles predictions and in situ experimental validation of alumina atomic layer deposition on metal surfaces. *Chemistry of Materials* **26**, 6752–6761 (2014).

25. Yao, Y., Fu, Q., Wang, Z., Tan, D. & Bao, X. Growth and characterization of two-dimensional FeO nanoislands supported on Pt(111). *Journal of Physical Chemistry C* **114**, 17069–17079 (2010).
26. Surnev, S. *et al.* Growth and structure of ultrathin vanadium oxide layers on Pd¹¹¹.... *Phys Rev B* **61**, 13945–13954 (2000).
27. Kale, M. J. & Christopher, P. Utilizing Quantitative in Situ FTIR Spectroscopy to Identify Well-Coordinated Pt Atoms as the Active Site for CO Oxidation on Al₂O₃-Supported Pt Catalysts. *ACS Catal* **6**, 5599–5609 (2016).
28. Zhou, J. *et al.* The role of the metal core in the performance of WO_x inverse catalysts. *Chem Catalysis* **3**, 1–17 (2023).
29. Wu, Y. *et al.* Dynamic Formation of Brønsted Acid Sites over Supported WO_x/Pt on SiO₂ Inverse Catalysts—Spectroscopy, Probe Chemistry, and Calculations. *ACS Catal* **13**, 7371–7382 (2023).
30. Sumaria, V. & Sautet, P. CO organization at ambient pressure on stepped Pt surfaces: First principles modeling accelerated by neural networks. *Chem Sci* **12**, 15543–15555 (2021).
31. Deshpande, S., Maxson, T. & Greeley, J. Graph theory approach to determine configurations of multidentate and high coverage adsorbates for heterogeneous catalysis. *NPJ Comput Mater* **6**, 1–6 (2020).
32. Ghanekar, P. G., Deshpande, S. & Greeley, J. Adsorbate chemical environment-based machine learning framework for heterogeneous catalysis. *Nat Commun* **13**, 1–12 (2022).
33. Deshpande, S. & Vlachos, D. G. A Data and DFT-Driven Framework for Predicting the Microstructure of Submonolayer Inverse Metal Oxide on Metal Catalysts. *J Phys Chem Lett* **15**, 2715–2722 (2024).
34. Wang, J. G. *et al.* One-dimensional PtO₂ at Pt steps: Formation and reaction with CO. *Phys Rev Lett* **95**, 1–4 (2005).
35. Feibelman, P. J., Esch, S. & Michely, T. O Binding Sites on Stepped Pt(111) Surfaces. *Phys Rev Lett* **77**, 2257–2260 (1996).
36. Schoiswohl, J. *et al.* Metal supported oxide nanostructures: Model systems for advanced catalysis. *Top Catal* **46**, 137–149 (2007).
37. Kumar, R. & Singh, A. K. Chemical hardness-driven interpretable machine learning approach for rapid search of photocatalysts. *NPJ Comput Mater* **7**, 1–13 (2021).
38. Chen, T. & Guestrin, C. XGBoost: A scalable tree boosting system. in *Proceedings of the ACM SIGKDD International Conference on Knowledge Discovery and Data Mining* vols 13-17-August-2016 785–794 (Association for Computing Machinery, 2016).
39. xgboost developers. Python API Reference. (2022).
40. Lei, Y. *et al.* Adsorbate-induced structural changes in 1-3 nm platinum nanoparticles. *J Am Chem Soc* **136**, 9320–9326 (2014).
41. Koningsberger, D. C. & Sayers, D. E. AN EXAFS STUDY OF PLATINUM-OXYGEN BONDS IN THE METAL-SUPPORT INTERFACE OF A HIGHLY Pt/Al₂O₃ CATALYST. DISPERSED. *Solid State Ion* **16**, 23–27 (1985).
42. Ramana, C. V., Utsunomiya, S., Ewing, R. C., Julien, C. M. & Becker, U. Structural stability and phase transitions in WO₃ thin films. *Journal of Physical Chemistry B* **110**, 10430–10435 (2006).

43. Diehl, R., Brandt, G. & Salje, E. The Crystal Structure of Triclinic WO₃. *Acta Crystallography* **34**, 1105–1111 (1978).
44. Huang, X., Zhai, H. J., Li, J. & Wang, L. S. On the structure and chemical bonding of tungsten oxide clusters W₃O_n⁻ and W₃O_n (n = 7-10): W₃O₈ as a potential molecular model for O-deficient defect sites in tungsten oxides. *Journal of Physical Chemistry A* **110**, 85–92 (2006).
45. Miller, J. T., Schreier, M., Kropf, A. J. & Regalbuto, J. R. A fundamental study of platinum tetraammine impregnation of silica: 2. The effect of method of preparation, loading, and calcination temperature on (reduced) particle size. *J Catal* **225**, 203–212 (2004).
46. Asokan, C., Xu, M., Dai, S., Pan, X. & Christopher, P. Synthesis of Atomically Dispersed Rh Catalysts on Oxide Supports via Strong Electrostatic Adsorption and Characterization by Cryogenic Infrared Spectroscopy. *The Journal of Physical Chemistry C* **126**, 18704–18715 (2022).
47. Zakem, G., Ro, I., Finzel, J. & Christopher, P. Support functionalization as an approach for modifying activation entropies of catalytic reactions on atomically dispersed metal sites. *J Catal* **404**, 883–896 (2021).
48. Nie, L. & Resasco, D. E. Kinetics and mechanism of m-cresol hydrodeoxygenation on a Pt/SiO₂ catalyst. *J Catal* **317**, 22–29 (2014).
49. Zhang, X., Tang, W., Zhang, Q., Wang, T. & Ma, L. Hydrocarbons Production from Lignin-derived Phenolic Compounds over Ni/SiO₂ Catalyst. *Energy Procedia* **105**, 518–523 (2017).
50. Barton, D. G., Shtein, M., Wilson, R. D., Soled, S. L. & Iglesia, E. Structure and electronic properties of solid acids based on tungsten oxide nanostructures. *Journal of Physical Chemistry B* **103**, 630–640 (1999).
51. Ross-Medgaarden, E. I. & Wachs, I. E. Structural determination of bulk and surface tungsten oxides with UV-vis diffuse reflectance spectroscopy and raman spectroscopy. *Journal of Physical Chemistry C* **111**, 15089–15099 (2007).
52. Yang, F. *et al.* Elucidating the Structure of Bimetallic NiW/SiO₂ Catalysts and Its Consequences on Selective Deoxygenation of m-Cresol to Toluene. *ACS Catal* **11**, 2935–2948 (2021).
53. Zaki, M. I., Hasan, M. A. & Pasupulety, L. Influence of CuOx additives on CO oxidation activity and related surface and bulk behaviours of Mn₂O₃, Cr₂O₃ and WO₃ catalysts. *Appl Catal A Gen* **198**, 247–259 (2000).
54. Meunier, F. C., Elgayyar, T., Dembélé, K. & Kaper, H. Stability of Pt-Adsorbed CO on Catalysts for Room Temperature-Oxidation of CO. *Catalysts* **12**, 1–12 (2022).
55. Tang, H. *et al.* Oxidative strong metal-support interactions (OMSI) of supported platinum-group metal catalysts. *Chem Sci* **9**, 6679–6684 (2018).
56. Song, T. *et al.* Oxidative strong metal-support interactions between metals and inert boron nitride. *Journal of Physical Chemistry Letters* **12**, 4187–4194 (2021).
57. Beck, A. *et al.* The dynamics of overlayer formation on catalyst nanoparticles and strong metal-support interaction. *Nat Commun* **11**, (2020).
58. Kale, M. J., Avanesian, T., Xin, H., Yan, J. & Christopher, P. Controlling catalytic selectivity on metal nanoparticles by direct photoexcitation of adsorbate-metal bonds. *Nano Lett* **14**, 5405–5412 (2014).

59. Darmawi, S. *et al.* Correlation of electrochromic properties and oxidation states in nanocrystalline tungsten trioxide. *Physical Chemistry Chemical Physics* **17**, 15903–15911 (2015).
60. Hotchandani, S., Bedja, I., Fessenden, R. W. & Kamat, P. V. Articles Electrochromic and Photoelectrochromic Behavior of Thin WOs Films Prepared from Quantum Size Colloidal Particles. *Langmuir* **10**, 17–22 (1994).
61. Baucke, F. G. K., Duffy, J. A. & Smith, R. I. OPTICAL ABSORPTION OF TUNGSTEN BRONZE THIN FILMS FOR ELECTROCHROMIC APPLICATIONS. *Thin Solid Films* **186**, 47–51 (1990).
62. Yamazaki, S. & Isoyama, K. Kinetic Studies of WO₃-Based Photochromism in Polyvinyl Alcohol Film. *Langmuir* **39**, 10240–10248 (2023).
63. Sangnier, A. *et al.* Thermokinetic and spectroscopic mapping of carbon monoxide adsorption on highly dispersed Pt/ γ -Al₂O₃. *ACS Catal* **11**, 13280–13293 (2021).
64. Hayden, B. E., Bradshaw, A. M. & Greenler, R. G. AN INFRARED STUDY OF THE ADSORPTION OF CO ON A STEPPED PLATINUM SURFACE. *Surf Sci* **149**, 394–406 (1985).
65. DeRita, L. *et al.* Structural evolution of atomically dispersed Pt catalysts dictates reactivity. *Nat Mater* **18**, 746–751 (2019).
66. Kappers, M. J. & Van Der Maas, J. H. Correlation between CO frequency and Pt coordination number. A DRIFT study on supported Pt catalysts. *Catal Letters* **10**, 365–374 (1991).
67. Lentz, C., Jand, S. P., Melke, J., Roth, C. & Kaghazchi, P. DRIFTS study of CO adsorption on Pt nanoparticles supported by DFT calculations. *J Mol Catal A Chem* **426**, 1–9 (2017).
68. Thang, H. V., Pacchioni, G., DeRita, L. & Christopher, P. Nature of stable single atom Pt catalysts dispersed on anatase TiO₂. *J Catal* **367**, 104–114 (2018).
69. DeRita, L. *et al.* Catalyst Architecture for Stable Single Atom Dispersion Enables Site-Specific Spectroscopic and Reactivity Measurements of CO Adsorbed to Pt Atoms, Oxidized Pt Clusters, and Metallic Pt Clusters on TiO₂. *J Am Chem Soc* **139**, 14150–14165 (2017).
70. Newton, M. A., Ferri, D., Smolentsev, G., Marchionni, V. & Nachttegaal, M. Room-temperature carbon monoxide oxidation by oxygen over Pt/Al₂O₃ mediated by reactive platinum carbonates. *Nat Commun* **6**, 1–7 (2015).
71. Derry, G. N. & Ross, P. N. HIGH COVERAGE STATES OF OXYGEN ADSORBED ON Pt(100) AND Pt(111) SURFACES. *Surf Sci* **140**, 165–180 (1984).
72. Ogawa, T., Kuwabara, A., Fisher, C. A. J., Moriwake, H. & Miwa, T. Adsorption and diffusion of oxygen atoms on a Pt(211) stepped surface. *Journal of Physical Chemistry C* **117**, 9772–9778 (2013).
73. Yue, J., Du, Z. & Shao, M. Mechanisms of Enhanced Electrocatalytic Activity for Oxygen Reduction Reaction on High-Index Platinum n(111)-(111) Surfaces. *Journal of Physical Chemistry Letters* **6**, 3346–3351 (2015).
74. Xu, J. & Yates, J. T. Catalytic oxidation of CO on Pt(335): A study of the active site. *J Chem Phys* **99**, 725–732 (1993).
75. Szabó, A., Henderson, M. A. & Yates, J. T. Oxidation of CO by oxygen on a stepped platinum surface: Identification of the reaction site. *J Chem Phys* **96**, 6191–6202 (1992).

76. Creighan, S. C., Mukerji, R. J., Bolina, A. S., Lewis, D. W. & Brown, W. A. The adsorption of CO on the stepped Pt{211} surface: a comparison of theory and experiment. *Catal Letters* **88**, 39–45 (2003).
77. Slavinskaya, E. M. *et al.* States of Pt/CeO₂ catalysts for CO oxidation below room temperature. *J Catal* **421**, 285–299 (2023).
78. Yoshinobu, J., Tsukahara, N., Yasui, F., Mukai, K. & Yamashita, Y. Lateral Displacement by Transient Mobility in Chemisorption of CO on Pt(997). *Phys Rev Lett* **90**, 1–4 (2003).
79. Toolenaar, F. J. C. M., Stoop, F. & Ponec', V. *On Electronic and Geometric Effects of Alloying An Infrared Spectroscopic Investigation of the Adsorption of Carbon Monoxide on Platinum-Copper Alloys. JOURNAL OF CATALYSIS* vol. 82 (1983).
80. Kim, C. S., Tornquist, W. J. & Korzeniewski, C. Site-dependent vibrational coupling of CO adsorbates on well-defined step and terrace sites of monocrystalline platinum: Mixed-isotope studies at Pt(335) and Pt(111) in the aqueous electrochemical environment. *J Chem Phys* **101**, 9112–9121 (1994).
81. Gautier, S., Steinmann, S. N., Michel, C., Fleurat-Lessard, P. & Sautet, P. Molecular adsorption at Pt(111). How accurate are DFT functionals? *Physical Chemistry Chemical Physics* **17**, 28921–28930 (2015).
82. Huang, X., Korányi, T. I., Boot, M. D. & Hensen, E. J. M. Ethanol as capping agent and formaldehyde scavenger for efficient depolymerization of lignin to aromatics. *Green Chemistry* **17**, 4941–4950 (2015).
83. Lindfors, C. Hydrodeoxygenation of lignin-derived phenol compound isoeugenol over nickel-and cobalt-based catalysts. (Abo Akademi University, Turku, 2019).
84. Tieuli, S. *et al.* Hydrodeoxygenation of isoeugenol over Ni-SBA-15: Kinetics and modelling. *Appl Catal A Gen* **580**, 1–10 (2019).
85. Bartolomei, E. *et al.* Lignin Depolymerization: A Comparison of Methods to Analyze Monomers and Oligomers. *ChemSusChem* **13**, 4633–4648 (2020).
86. Xiao, X. *et al.* The role of oxygen vacancies in biomass deoxygenation by reducible zinc/zinc oxide catalysts. *Catal Sci Technol* **8**, 1819–1827 (2018).
87. Goulas, K. A., Mironenko, A. V., Jenness, G. R., Mazal, T. & Vlachos, D. G. Fundamentals of C–O bond activation on metal oxide catalysts. *Nat Catal* **2**, 269–276 (2019).
88. Teles, C. A. *et al.* Role of the metal-support interface in the hydrodeoxygenation reaction of phenol. *Appl Catal B* **277**, 1–13 (2020).
89. Abreu Teles, C., Duong, N., Rabelo-Neto, R. C., Resasco, D. & Noronha, F. B. Evidence of dependence between the deoxygenation activity and metal-support interface. *Catal Sci Technol* **12**, 5961–5969 (2022).
90. Deo, S. & Janik, M. J. Predicting an optimal oxide/metal catalytic interface for hydrodeoxygenation chemistry of biomass derivatives. *Catal Sci Technol* **11**, 5606–5618 (2021).
91. Flores, A. F., Burwell, R. L. & Butt, J. 8. Structure Sensitivity of Benzene Hydrogenation on Supported Pt Catalysts. *Journal of the Chemical Society, Faraday Transactions* **88**, 1191–1196 (1992).
92. Kresse, G. & Furthmüller, J. Efficient iterative schemes for ab initio total-energy calculations using a plane-wave basis set. *Phys Rev B* **54**, 11169–11186 (1996).

93. Perdew, J. P., Burke, K. & Ernzerhof, M. Generalized Gradient Approximation Made Simple. *Phys Rev Lett* **77**, 3865–3868 (1996).
94. Kresse, G. & Joubert, D. From ultrasoft pseudopotentials to the projector augmented-wave method. *Phys Rev B* **59**, 1758–1775 (1999).
95. Scanlon, J. T. & Willis, D. E. Calculation of Flame Ionization Detector Relative Response Factors Using the Effective Carbon Number Concept. *J Chromatogr Sci* **23**, 333–340 (1985).

For Table of Contents Only

WO_x Decorates Pt in Site-Selective Manner

